Supplementary: Optimizing Under-Display ToF Imaging with Learnable Fractional Reaction-Diffusion Dynamics and Beyond

In this document, we provide additional details concerning "Optimizing Under-Display ToF Imaging with Learnable Fractional Reaction-Diffusion Dynamics and Beyond". Specifically, we provide more description and the mathematical basis for our proposal, exhaustive implementation details, and additional experimental results to further validate it.

A. Task Definition in Under-Display ToF Depth Restoration

The task of depth restoration in under-display Time-of-Flight (UD-ToF) imaging aims to recover accurate depth maps from degraded measurements captured through semi-transparent display panels, such as TOLED (Transparent OLED), as shown in Fig. 1. Compared with conventional ToF imaging, UD-ToF suffers from more complex and severe degradation due to the layered optical structure of the screen and imperfect light transmission.

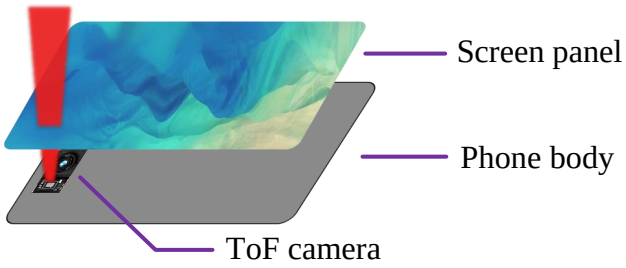

Figure 1. **Schematic of under-display ToF imaging.** The infrared signal passes through the screen twice, introducing attenuation and multipath interference before reaching the ToF sensor.

Specifically, the major sources of degradation include:

- **Multipath interference (MPI)**: Internal reflections within the display layers and glass cover can cause the IR signal to follow multiple paths, leading to biased depth estimations.
- **Spatially varying noise**: Due to the non-uniform transmittance and fabrication imperfections across the display panel, the noise distribution varies spatially, violating the i.i.d. assumption common in conventional ToF models.
- **Signal attenuation and low SNR**: The semi-transparent screen introduces substantial signal attenuation by absorbing and scattering infrared light, while also introducing additional noise due to its complex layered structure. As a result, the signal-to-noise ratio (SNR) decreases significantly, leading to degraded depth accuracy.

Formally, given a degraded depth observation $\mathbf{D}_{\text{raw}} \in \mathbb{R}^{H\times W}$ and auxiliary cues such as amplitude $\mathbf{A}$ or IR maps $\mathbf{I}$, the goal is to estimate a high-quality depth map $\mathbf{D}_{\text{ref}}$ that closely approximates the ground truth $\mathbf{D}_{\text{gt}}$. This estimation must not only correct local distortions and missing details caused by panel-induced degradation but also maintain global structural consistency across the scene. Furthermore, practical UD-ToF systems often operate under limited data and hardware constraints, making the design of robust, interpretable, and physically grounded restoration frameworks particularly critical.

B. More Description about Diffusion Process

In the main text, we have introduced the Perona-Malik (P-M) model. Here. we will utilize it as the foundational basis to facilitate the discussion of other related issues. Firstly, given the spatial information $\mathbf{z}$ on a bounded domain $\Omega \in \mathbb{R}^2$ and time t, the latent clear image $u(\mathbf{z})$ can be obtained by solving the equation

$$\begin{cases} \dfrac{\partial u}{\partial t} = \operatorname{div}(g|\nabla u|\nabla u), & (\mathbf{z}, t) \in \Omega \times (0, T] \\ u(\mathbf{z}, 0) = u_0(\mathbf{z}), & \mathbf{z} \in \Omega \end{cases} \tag{1}$$

with $u_0(\mathbf{z})$ being the initial condition, $g(\cdot)$ the diffusivity function and $u(\mathbf{z})$ the solution at time t.

Then we discretize the P-M model into a partial differential equation with an explicit finite difference scheme

$$\frac{u_{t+1}(\mathbf{z}) - u_t(\mathbf{z})}{\Delta t} = -\sum_{\mathbf{z}} \nabla_{\mathbf{z}}^{\top} \phi(\nabla_{\mathbf{z}} u_t(\mathbf{z})) \tag{2}$$

where Δt is the time step, $\nabla_{\mathbf{z}}$ is a finite difference approximation of the gradient operator, and $\phi(\nabla_{\mathbf{z}} u) = (\phi(\nabla_{\mathbf{z}} u)_1, \cdots, \phi(\nabla_{\mathbf{z}} u)_N^{\top})$ with the influence function $\phi(\eta) = \eta g(\eta)$. For simplicity, we denote $u_t(\mathbf{z})$ as u_t.

Based on Eq. 2, the update for the state u_{t+1} in the diffusion step can be expressed as

$$u_{t+1}^{p,q} = u_t^{p,q} - \Delta t \cdot \nabla_{\mathbf{z}}^{\top} \phi(\nabla_{\mathbf{z}} u_t) \tag{3}$$

where $(p.q)$ is the central pixel to be updated.

Eq. 3 illustrates that the predicted state u_{t+1} in the diffusion process depends solely on the current state u_t.

On the other hand, the update operation for each pixel is essentially a weighted average of its neighboring pixels. With the neighborhood-based difference approximation, the updated formula can be expressed as

$$\begin{aligned} u_{t+1}^{p,q} &= u_t^{p,q} - \Delta t \cdot \sum_{m,n \in \mathcal{N}} \phi(\nabla_{\mathbf{z}} u_t) \cdot (u_t^{m,n} - u_t^{p,q}) \\ &= u_t^{p,q} - \Delta t \cdot \sum_{k \in \mathcal{N}} g_k \cdot \delta u_t^k \end{aligned} \tag{4}$$

where $\delta u_t^k = u_t^{m,n} - u_t^{p,q}$, and $k = (m,n) \in \mathcal{N}$ can be the 4-neighborhood or 8-neighborhood, even other neighborhood patterns.

From Eq. 4, it can be observed that *each diffusion step can be regarded as a discrete convolution operation*. This operation uses a kernel to perform a dot product with a local region of the image, generating a new pixel value. The choice of kernel and its weights can be designed according to the diffusion equation to control the diffusion rate and direction. As a result, discrete convolution is commonly employed in an implementation to compute the diffusion process efficiently.

C. Theoretical Basis

C.1. Fractional Calculus

There exist several definitions for fractional derivatives, among which the Riemann-Liouville one [4, 6, 7] and the Caputo one [12] are usually considered in the control field. There also exists the Grünwald-Letnikov one [1] which coincides with the Riemann-Liouville one in many cases[11].

Physical and geometric interpretations of fractional derivatives can be found in [13] and the references cited therein. Moreover, the physical meaning of initial conditions with the Riemann-Liouville fractional derivative was explained in [5].

Through this section, let $I = [a,b] \subset \mathbb{R}$, $\alpha \in \mathbb{R}_+$, and $l = \lceil \alpha \rceil$, where $\lceil \alpha \rceil$ (resp. $\lfloor \alpha \rfloor$) denotes the smallest (resp. largest) integer greater than or equal to α. Then, all the definitions given in this section can be found in [8, 11]. In this section, we will introduce some fundamental functions which play an important role in fractional calculus.

C.2. Gamma Function

Like the factorial operator which plays an indispensable role in classical calculus, the Gamma function is one of the most fundamental tools in fractional calculus. It was first introduced by the famous mathematician Leonhard Euler as a natural extension of the factorial operator from positive integers to real numbers [3].

Definition 1. *[9] The Gamma function is defined by: $\forall\, x \in \mathbb{C}^* \setminus \mathbb{Z}_-$,*

$$\Gamma(x) = \int_0^{\infty} t^{x-1} e^{-t} dt. \tag{5}$$

C.3. Riemann-Liouville fractional integrals and derivatives

Let us begin this subsection with the following definition.

Definition 2. *The Riemann-Liouville fractional integral of a function f is defined as follows: $\forall\, t > a$,*

$$\begin{cases} \mathrm{D}_{a,t}^{0} f(t) & := f(t), \\ \mathrm{D}_{a,t}^{-\alpha} f(t) & := \dfrac{1}{\Gamma(\alpha)} \displaystyle\int_a^t (t-\tau)^{\alpha-1} f(\tau)\, d\tau. \end{cases} \tag{6}$$

Remark that if f is continuous for $t \geq 0$, we have $\lim\limits_{\alpha \to 0} \mathrm{D}_{a,t}^{-\alpha} f(t) = \mathrm{D}_{a,t}^{0} f(t) = f(t)$ [11].

By taking integer numbers in (6), we can obtain the following Cauchy formula: $\forall\, n \in \mathbb{N}^*$,

$$\mathrm{D}_{a,t}^{-n} f(t) = \frac{1}{(n-1)!} \int_a^t (t-\tau)^{n-1} f(\tau) d\tau, \tag{7}$$

which refers to the n^{th} order integral from a to t.

The Riemann-Liouville fractional integral of f can also be interpreted as the convolution product of $\frac{t^{\alpha-1}}{\Gamma(\alpha)}$ and f: $\forall\, t > a$,

$$\mathrm{D}_{a,t}^{-\alpha} f(t) = x_{[a,+\infty[} \frac{t^{\alpha-1}}{\Gamma(\alpha)} * f(t), \tag{8}$$

where $*$ stands for the convolution product, $\frac{t^{\alpha-1}}{\Gamma(\alpha)}$ is usually called the kernel of the fractional integral operator, where $x_{[a,+\infty[}$ is the indicator function of the interval $[a,+\infty[$. Thus, the function is assumed to be 0 for $t < a$ (causality).

Based on the R-L fractional integrals, the fractional derivatives can be defined by applying the integer order derivative operator.

Definition 3. *The Riemann-Liouville fractional derivative of a function f is defined as follows: $\forall\, t > a$,*

$$\mathrm{D}_{a,t}^{\alpha} f(t) := \frac{d^l}{dt^l} \left\{ \mathrm{D}_{a,t}^{\alpha-l} f(t) \right\}. \tag{9}$$

Module	Name	Layer	Kernel	Stride	In / Out	Input
Coefficients Prediciton	conv1	Conv2D + GeLU	3	1	51 / 32	*feat_in*
	conv2	Conv2D	3	1	32 / 32	conv1
	feat_out	Conv2D	3	1	32 / 18	*feat_in*[0:32] + *conv2*

Table 1. Network architecture for coefficient prediction in continuous convolution.

C.4. Caputo fractional derivatives

Different from the R-L fractional derivative, the Caputo fractional derivative is defined by taking the R-L fractional integral of an integer order derivative.

Definition 4. *The Caputo fractional derivative of f is defined as follows:*
$\forall\, t \in]a, +\infty[$,

$$ {}^{C}\mathrm{D}^{\alpha}_{a,t} f(t) := \frac{1}{\Gamma(l-\alpha)} \int_a^t (t-\tau)^{l-\alpha-1} f^{(l)}(\tau)\, d\tau. \tag{10} $$

The upper-left index C in ${}^{C}\mathrm{D}^{\alpha}_{a,t} f$ is used to distinguish from the R-L fractional derivative. The relationship between these two fractional derivatives is established in the following formulae.

• If $-1 < \alpha < 0$, then $l = 0$. We have:

$$ \mathrm{D}^{\alpha}_{a,t} f(t) = {}^{C}\mathrm{D}^{\alpha}_{a,t} f(t). \tag{11} $$

• If $\alpha \in \mathbb{R}_+ \setminus \mathbb{N}$, then $l \in \mathbb{N}^*$. We have [11]:

$$ {}^{C}\mathrm{D}^{\alpha}_{a,t} f(t) = \mathrm{D}^{\alpha}_{a,t} f(t) - \sum_{i=0}^{l-1} \frac{(t-a)^{i-\alpha}}{\Gamma(i+1-\alpha)} f^{(i)}(a). \tag{12} $$

C.5. Grünwald-Letnikov fractional derivative

Let us introduce the last fractional derivative, which is particularly useful in this article.

Definition 5. *The Grünwald-Letnikov fractional derivative of a function f is given by: $\forall\, t > a$,*

$$ {}^{GL}\mathrm{D}^{\alpha}_{a,t} f(t) := \lim_{h \to 0} h^{-\alpha} \sum_{j=0}^{\lceil \frac{t-a}{h} \rceil} (-1)^j \binom{\alpha}{j} f(t-jh), \tag{13} $$

where $\binom{\alpha}{j} = \dfrac{\Gamma(\alpha+1)}{\Gamma(\alpha+1-j)j!}$ is the generalized binomial coefficient.

The Grünwald-Letnikov scheme is usually used to approximate the Riemann-Liouville and Caputo fractional integrals and derivatives in discrete cases.

The choice of the Caputo derivative over others in many real-world applications, especially in engineering and physics, is often made due to its ability to incorporate initial conditions that resemble those used in traditional integer-order differential equations. These initial conditions are generally understood and interpreted in a straightforward manner within established theoretical frameworks.

C.6. Determination of the fractional orders

The study [2] investigates the determination of the fractional order α in subdiffusion equations and proves that under appropriate initial conditions, boundary constraints, and additional observation constraints, the fractional order is uniquely determined. The existence of a solution to the inverse problem is ensured when an appropriate observation constraint is provided. Specifically, the integral condition

$$ \int_\Omega u(x, t_0) v_1(x) dx = d_0 \neq 0 \tag{14} $$

guarantees that a valid fractional order can be determined. The function $v_1(x)$ represents the first eigenfunction of the associated elliptic operator, ensuring that the constraint is well-posed within the problem's functional framework.

Uniqueness of the solution is established under additional restrictions. If the initial function satisfies the required regularity conditions and the first eigenvalue of the spectral problem is zero ($\lambda_1 = 0$), then the fractional order α is uniquely determined. The condition

$$ 0 < \frac{d_0}{\varphi_1} < 1 \tag{15} $$

ensures that no multiple values of α satisfy the given integral constraint. In cases where noise is present in the observations, the stability of numerical methods may be affected, but the fundamental existence and uniqueness results remain valid. Regularization techniques can be applied to mitigate numerical instability while preserving the well-posed nature of the inverse problem.

D. Detailed Implementation Settings

We chose UD-ToFnet as our baseline network, but we slightly modified its final convolutional layer to implement our iterative optimization scheme. Specifically, we leverage three convolution layers to generate depth features F. The code for the deep fractional reaction-diffusion model is adapted from NLSPN [10], with hyperparameter settings

also referenced from it. For instance, the number of iterations is set to 6. Moreover, the confidence propagation scheme within it is retained as an optional feature. To generate confidence maps, we also employ three convolutional layers, taking the amplitude map derived from ToF raw measurements as input. All the aforementioned convolutional operations utilize hidden layers with 32 channels to reduce the number of parameters. The approach to generating fractional orders aligns with that of generating confidence maps.

On the other hand, due to the presence of singularities in the Caputo fractional differential equations, the network frequently encounters NaN values during training, leading to interruptions. To mitigate the problem, we restrict the fractional order within the range of [0.1, 0.9].

In addition, we provide the detailed neural network structure for coefficient prediction of continuous convolution as reported in Table 1. During the training process, we set two depth losses for the initial depth u_0 and the final depth u_6, which are defined as:

$$L_d = \| (\tilde{u}_6 - u_{gt}) \odot \mathbb{I} \|_1 + \lambda_d \cdot \| (\tilde{u}_0 - u_{gt}) \odot \mathbb{I} \|_1 \quad (16)$$

where $\mathbb{I}$ is pixel validity. Empirically, we set $\lambda_d = 0.1$.

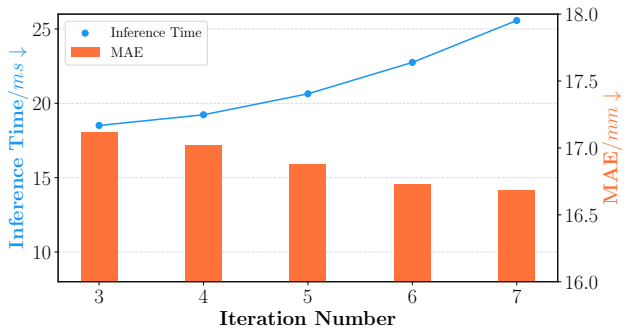

Figure 2. **Ablation study – Iteration Number.** Comparison between models with different iteration numbers.

E. Additional Experimental Results

E.1. Effect of Iteration Number

This section demonstrates how model performance and inference times vary with different iteration numbers. As shown in Fig. 2, since our method exhibits long-term memory, where each current state is correlated with previous iterations, the inference time increases exponentially and the MAE metric gradually exhibits a downward trend, as the iteration number grows. In particular, we observe fluctuations in MAE when the iteration number is relatively low, specifically, in the vicinity of iteration 5. In our experiments, we set the iteration number to 6 to balance achieving satisfactory metric performance and maintaining acceptable inference times.

E.2. Qualitative Results at Different Iterations

Here, we provide additional qualitative results at different iterations. In Fig. 3, as the iteration number increases, depth consistently and progressively approximates the ground truth depth, indicating a steady improvement in accuracy toward the desired outcome.

E.3. Qualitative Effect of Variable Order Selection

To validate the effectiveness of the variable fractional order, we project the order of each pixel onto a 2D image. As shown in Fig. 4, we discern that the order maps undergo pronounced variations in regions with distinct gradient changes, particularly along the edges of portrait and facial models, while remaining relatively stable in flat regions. This further demonstrates that the proposed method is capable of accurately restoring depth while preserving fine-grained details.

E.4. Qualitative Comparison with State-of-the-art Approaches

Here, we report further qualitative comparison results on the two UD-ToF datasets, the FLAT dataset and the NYUv2 dataset. As shown in Fig. 5-7, our network produces fewer errors when recovering fine structures and high-frequency details.

References

[1] Sergey Abrashov, Rachid Malti, Mathieu Moze, Xavier Moreau, Francois Aioun, and Franck Guillemard. Simple and robust experiment design for system identification using fractional models. *IEEE Transactions on Automatic Control*, 2016. 2

[2] Ravshan Ashurov and Sabir Umarov. Determination of the order of fractional derivative for subdiffusion equations. *Fractional Calculus and Applied Analysis*, 23(6): 1647–1662, 2020. 3

[3] Philip J Davis. Leonhard euler's integral: A historical profile of the gamma function: In memoriam: Milton abramowitz. *The American Mathematical Monthly*, 66(10): 849–869, 1959. 2

[4] Said Djennoune and Maamar Bettayeb. Optimal synergetic control for fractional-order systems. *Automatica*, 49(7): 2243–2249, 2013. 2

[5] Nicole Heymans and Igor Podlubny. Physical interpretation of initial conditions for fractional differential equations with riemann-liouville fractional derivatives. *Rheologica Acta*, 45 (5):765–771, 2006. 2

[6] Salim Ibrir and Maamar Bettayeb. New sufficient conditions for observer-based control of fractional-order uncertain systems. *Automatica*, 59:216–223, 2015. 2

[7] Shyam Kamal, Arun Raman, and Bijnan Bandyopadhyay. Finite-time stabilization of fractional order uncertain chain of integrator: an integral sliding mode approach. *IEEE Transactions on Automatic Control*, 58(6):1597–1602, 2013. 2

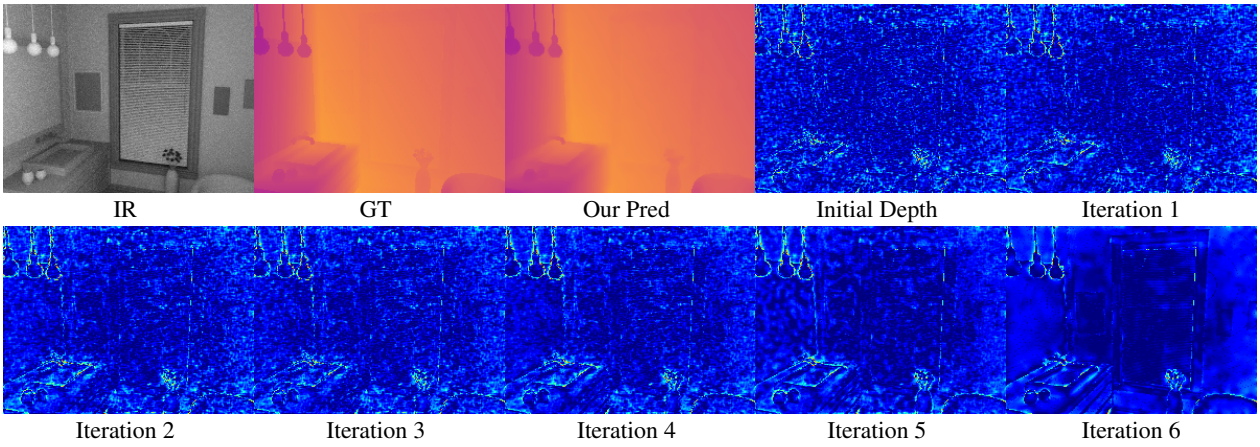

Figure 3. **Qualitative results of different iterations.** IR, GT, and Our Pred represent IR image, ground-truth depth, and depth map predicted by LFRD^2. Iteration i denotes the error map after i-th iteration.

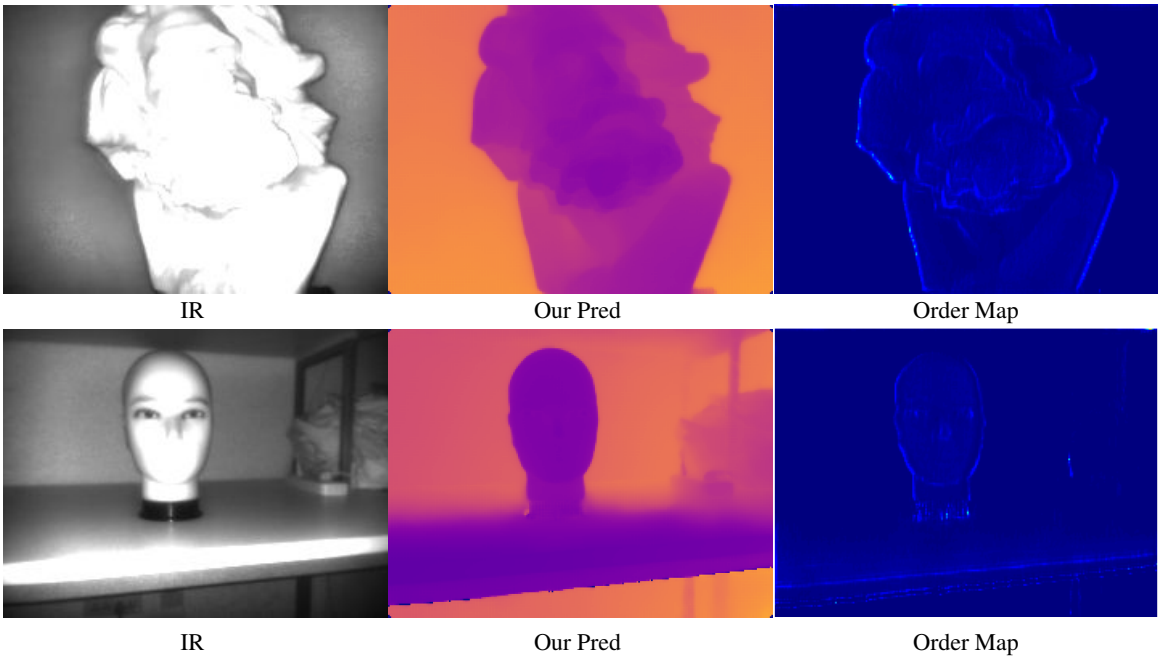

Figure 4. **Qualitative results of order maps.** IR and Our Pred represent IR image and depth map predicted by LFRD^2.

[8] Anatoly A Kilbas, Hari M Srivastava, and Juan J Trujillo. Theory and applications of fractional differential equations, 2006. 2

[9] Kenneth S Miller and Bertram Ross. An introduction to the fractional calculus and fractional differential equations. 1993. 2

[10] Jinsun Park, Kyungdon Joo, Zhe Hu, Chi-Kuei Liu, and In So Kweon. Non-local spatial propagation network for depth completion. In *Computer Vision–ECCV 2020: 16th European Conference, Glasgow, UK, August 23–28, 2020, Proceedings, Part XIII 16*, pages 120–136. Springer, 2020. 3

[11] Igor Podlubny. *Fractional differential equations: an introduction to fractional derivatives, fractional differential equations, to methods of their solution and some of their applications*. Academic press, 1998. 2, 3

[12] Xiaojun Tang, Yang Shi, and Li-Lian Wang. A new framework for solving fractional optimal control problems using fractional pseudospectral methods. *Automatica*, 78:333–340, 2017. 2

[13] Vasily E Tarasov. Geometric interpretation of fractional-order derivative. *Fractional Calculus and Applied Analysis*, 19(5):1200–1221, 2016. 2

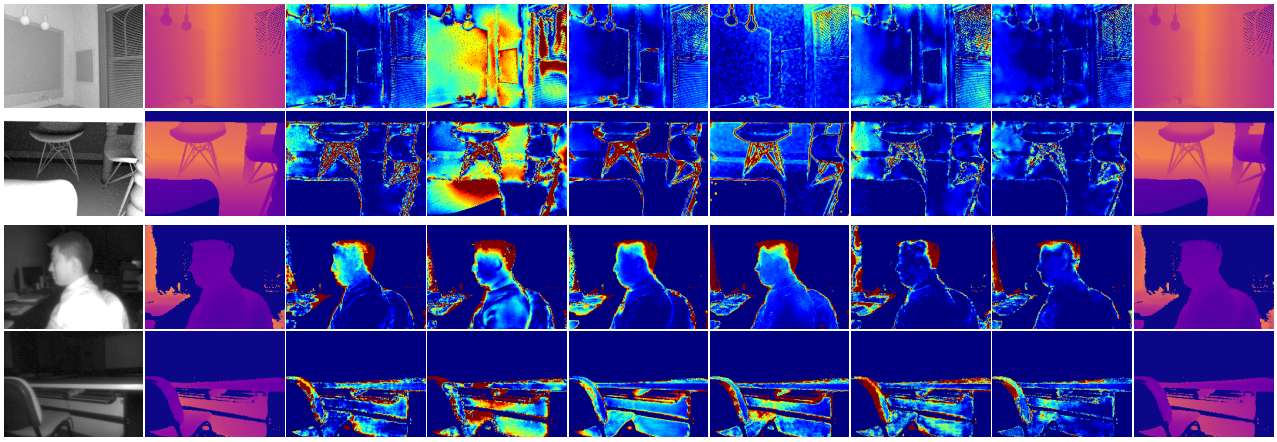

(a) IR **(b)** GT **(c)** PE-ToF **(d)** SHARPnet **(e)** Restormer **(f)** NAFNet **(g)** UD-ToFnet **(h)** Ours **(i)** Ours Pred

Figure 5. **Qualitative results on SUD-ToF dataset.** From left to right: (a) IR image and (b) ground-truth depth, followed by (c-g) error maps achieved by state-of-the-art solutions and (h) LFRD^2, (i) depth maps predicted by LFRD^2.

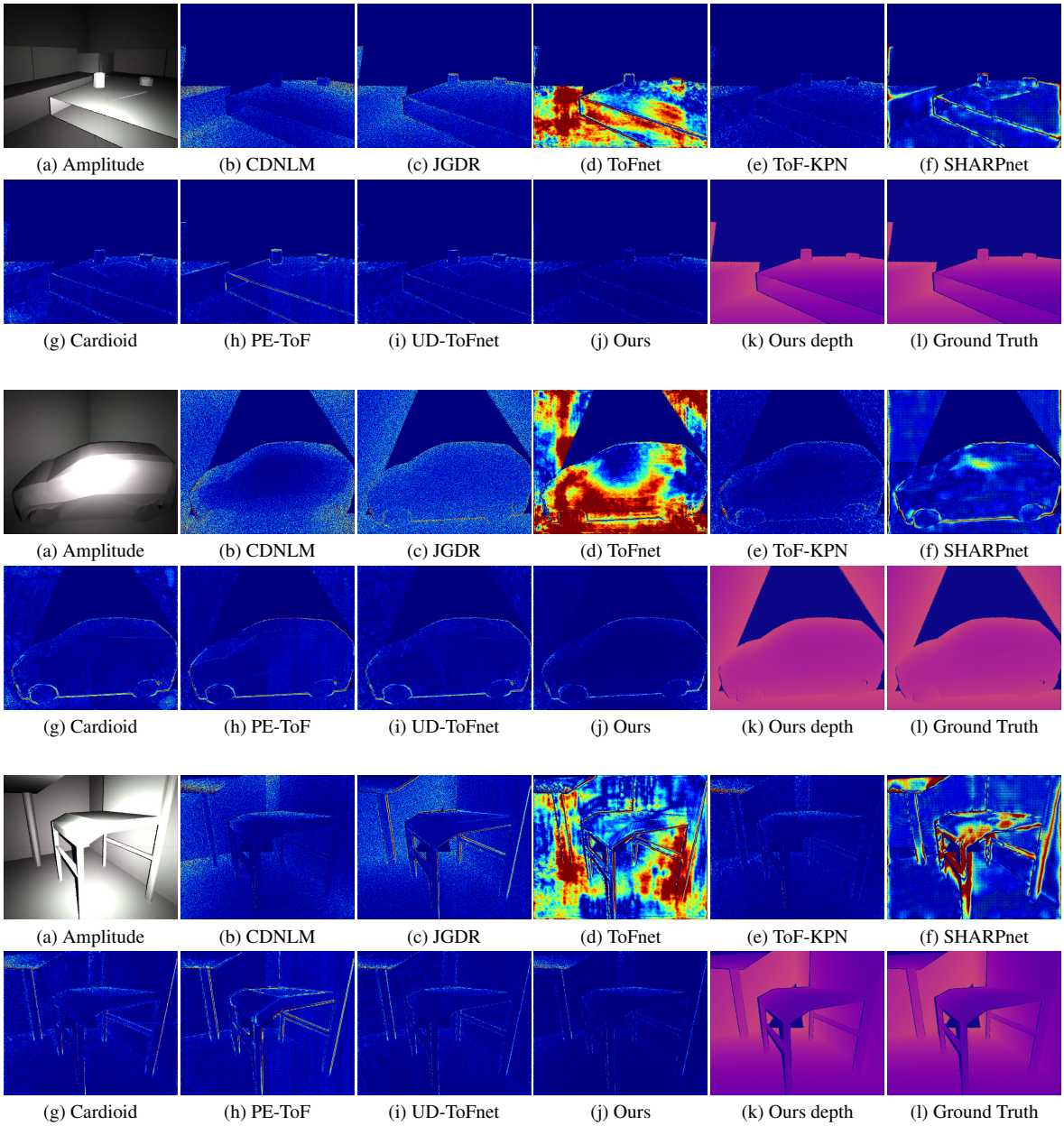

Figure 6. Qualitative results on the FLAT dataset. From left to right, the first column is (a) Amplitude maps; (b)-(i) are error maps of selected methods; the last three columns are (j) the error map of our method, (k) the prediction generated from our method and (l) the ground truth depth.

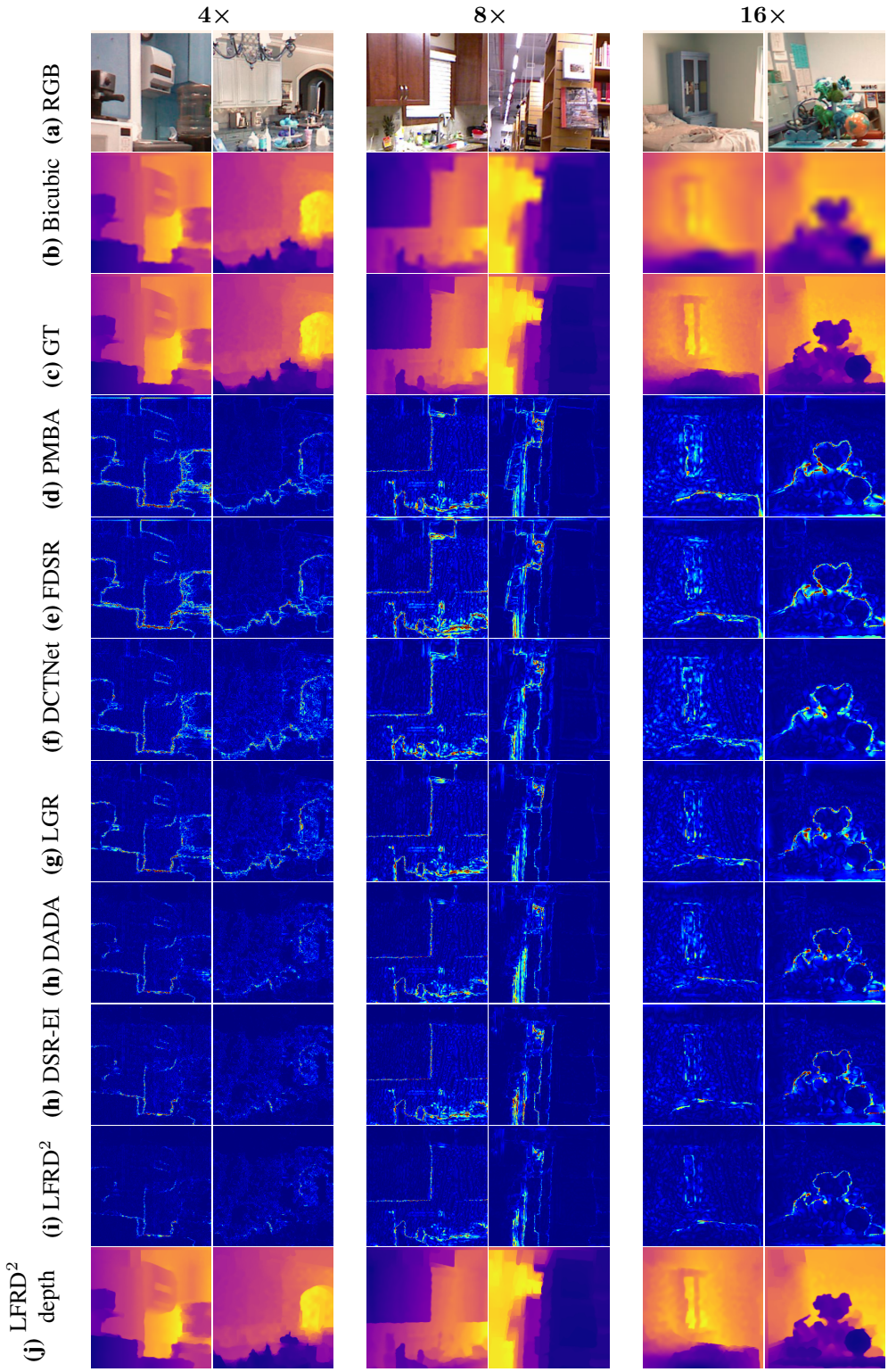

Figure 7. **Qualitative comparison on the NYUv2 dataset.** From top to bottom: (a) RGB image, (b) Bicubic upsampled depth map, (c) GT; then, (d)-(h) are error maps achieved by selected methods; finally, (i) error maps and (j) predictions by LFRD^2.